

# Void Formation and Roughening in Slow Fracture

Itai Afek, Eran Bouchbinder, Eytan Katzav, Joachim Mathiesen and Itamar Procaccia  
*Dept. of Chemical Physics, The Weizmann Institute of Science, Rehovot 76100, Israel*

Slow crack propagation in ductile, and in certain brittle materials, appears to take place via the nucleation of voids ahead of the crack tip due to plastic yields, followed by the coalescence of these voids. Post mortem analysis of the resulting fracture surfaces of ductile and brittle materials on the  $\mu\text{m}$ -mm and the nm scales respectively, reveals self-affine cracks with anomalous scaling exponent  $\zeta \approx 0.8$  in 3-dimensions and  $\zeta \approx 0.65$  in 2-dimensions. In this paper we present an analytic theory based on the method of iterated conformal maps aimed at modelling the void formation and the fracture growth, culminating in estimates of the roughening exponents in 2-dimensions. In the simplest realization of the model we allow one void ahead of the crack, and address the robustness of the roughening exponent. Next we develop the theory further, to include two voids ahead of the crack. This development necessitates generalizing the method of iterated conformal maps to include doubly connected regions (maps from the annulus rather than the unit circle). While mathematically and numerically feasible, we find that the employment of the stress field as computed from elasticity theory becomes questionable when more than one void is explicitly inserted into the material. Thus further progress in this line of research calls for improved treatment of the plastic dynamics.

## I. INTRODUCTION

In this paper we expand on the results of a recent Letter [1] in which a model was proposed for slow crack propagation via void formation ahead of the crack due to plastic yields. Here ‘slow’ means propagation velocity considerably smaller than the Rayleigh wave speed. The model was motivated by some quantitative studies of fracture surfaces, which reveal self-affine rough cracks with two scaling regimes: at small length scales (smaller than a typical cross-over length  $\xi_c$ ) the roughness exponent is  $\zeta \approx 0.5$ , whereas at scales larger than  $\xi_c$  the roughness exponent is  $\zeta \approx 0.8$ . The second scaling regime is seen to have an upper cut-off  $\xi$  known as the correlation length. Such measurements were reported first for ductile materials (like metals) where  $\xi_c$  is of the order of  $1 \mu\text{m}$  [2, 3], and more recently for brittle materials like glass, but with a much smaller value of  $\xi_c$ , of about  $1 \text{ nm}$  [4]. Similar experiments conducted on 2-dimensional samples reported rough cracks with large-scale exponents  $\zeta \approx 0.65 \pm 0.04$  [5, 6, 7]. The exponent  $\zeta \approx 0.5$  is characteristic of uncorrelated random surfaces, but higher exponents indicate the existence of positive correlations [8]; naturally, the experimental discovery of such correlated “anomalous” exponents attracted considerable interest with repeated attempts to derive them theoretically [9, 10, 11]. Ref. [1] presented a quantitative model for self-affine fracture surfaces based on elasticity theory supplemented with considerations of plastic deformations. Focussing on infinite 2-dimensional materials, Ref. [1] followed the qualitative picture presented recently in [12], see Fig. 1. In this picture there exists a “process zone” in front of the crack tip in which plastic yield is accompanied by the evolution of damage cavities. A crucial aspect of this picture is the existence of a typical scale,  $\xi_c$ , which is roughly the distance between the crack tip and the first void, at the time of the nucleation of the latter. The voids are nucleated under the influence of the stress field  $\sigma_{ij}(\mathbf{r})$  adjacent to the tip, but not *at* the tip, due to the existence of the plastic

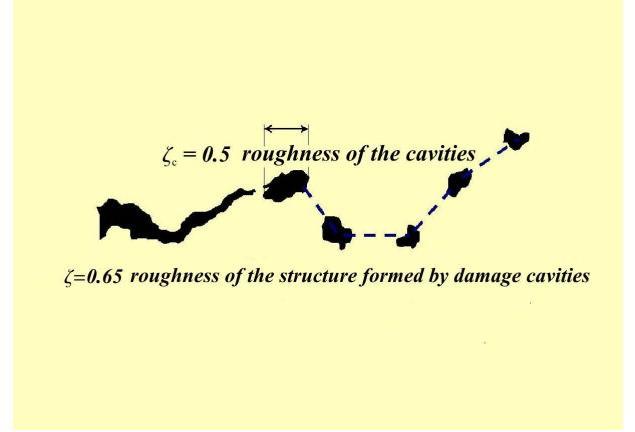


FIG. 1: The fracture scenario suggested in [12]. This scenario had been documented in detail in corrosive glass fracture, and also more recently in the fracture of paper [13].

zone that cuts off the purely linear-elastic (unphysical) crack-tip singularities. The crack grows by coalescing the voids with the tip, creating a new stress field which induces the nucleation of new voids. In the picture of [12] the scale  $\xi_c$  is also identified with the typical size of the voids at coalescence. A consequence of this picture is that the roughening exponent  $\zeta \approx 0.5$  corresponds to the surface structure of individual voids, whereas the large-scale anomalous exponent has to do with the correlation between the positions of different voids that coalesce to constitute the evolving crack. Ref. [1] provided first a theory for the scale  $\xi_c$  and second, demonstrated that the positions of consecutive voids are positively correlated. In this paper we amplify on these results.

In Sect. II we discuss again the model of Ref. [1], expand the theoretical presentation, and test the robustness of the roughening exponent that this model predicts. Since the roughening exponent found is larger than 0.5, this indicates the existence of positive correlations be-

tween crack increments. To illuminate these long range correlation we demonstrate in Sect. III that the analytic structure of the theory dictates the existence of power-law correlations between height fluctuations in the crack and the value of the mode II stress intensity factor  $K_{II}$  at the tip. In Sect. IV we construct a model with two voids ahead of the crack. After setting up the problem, we describe in some detail the mathematical apparatus that employs conformal maps from the annulus to the doubly connected region of a crack with a void which allows the computation of the stress field around such a configuration. In Sect. V we present results of the two-void model, and discuss the relevance of the results to the growth and roughening of cracks. The conclusion is that since the details of plastic deformations are not well understood the physics of crack growth is better described by the one-void model than the two-void model; the stress field computed for a crack with one void ahead is physically acceptable as long as elasticity theory is relevant, but when the first void appears due to plastic events a correct determination of the stress field should include a better handling of the plastic zone. This must await future improvement of our understanding of plastic dynamics.

## II. ONE-VOID MODEL

### A. The plastic zone and void nucleation

A simple model for  $\xi_c$  can be developed by assuming the process zone to be properly described by the Huber-von Mises plasticity theory [14]. This theory focuses on the deviatoric stress  $s_{ij} \equiv \sigma_{ij} - \frac{1}{3}\text{Tr}\sigma\delta_{ij}$  and on its invariants. The second invariant,  $J_2 \equiv \frac{1}{2}s_{ij}s_{ij}$ , corresponds to the distortional energy. The material yields as the distortional energy exceeds a material-dependent threshold  $\sigma_Y^2$ . The fact that we treat this threshold as a constant, independent of the state of deformation and its history, implies that we specialize for “perfect” plasticity. In 2-dimensions this yield condition reads [14]

$$J_2 = \frac{\sigma_1^2 - \sigma_1\sigma_2 + \sigma_2^2}{3} = \sigma_Y^2. \quad (1)$$

Here  $\sigma_{1,2}$  are the principal stresses given by

$$\sigma_{1,2} = \frac{\sigma_{yy} + \sigma_{xx}}{2} \pm \sqrt{\frac{(\sigma_{yy} - \sigma_{xx})^2}{4} + \sigma_{xy}^2}. \quad (2)$$

In the purely linear-elastic solution the crack-tip region is where high stresses are concentrated (in fact diverging near a sharp tip). Perfect plasticity implies on the one hand that the tip is blunted, and on the other hand that inside the plastic zone the Huber-von Mises criterion (1) is satisfied. The outer boundary of the plastic zone will be called below the “yield curve”, and in polar coordinates around the crack tip will be denoted  $R(\theta)$ .

Whatever is the actual shape of the blunted tip its boundary cannot support normal components of the stress. Together with Eq. (1) this implies that on the crack interface

$$\sigma_1 = \sqrt{3}\sigma_Y, \quad \sigma_2 = 0. \quad (3)$$

On the other hand, the linear-elastic solution, which is still valid outside the plastic zone, imposes the outer boundary conditions on the yield curve. Below we will compute the outer stress field *exactly* for an arbitrarily shaped crack using the recently developed method of iterated conformal mappings [15]. For the present argument we will take the outer stress field to conform with the universal linear-elastic stress field for mode I symmetry,

$$\sigma_{ij}(r, \theta) = \frac{K_I}{\sqrt{2\pi r}} \Sigma_{ij}^I(\theta). \quad (4)$$

For a crack of length  $L$  with  $\sigma^\infty$  being the tensile load at infinity, the stress intensity factor  $K_I$  is expected to scale like  $K_I \sim \sigma^\infty \sqrt{L}$ . Using this field we can find the yield curve  $R(\theta)$ . Typical yield curves for straight and curved cracks are shown in the insets of Figs. 3 and 6.

The typical scale  $\xi_c$  follows from the physics of the nucleation process. It is physically plausible that void formation is more susceptible to the growth of hydrostatic tension than to distortional stresses. We assume that void nucleation occurs where the hydrostatic tension  $P$ ,  $P \equiv \frac{1}{2}\text{Tr}\sigma$ , exceeds some threshold value  $P_c$ . The hydrostatic tension increases when we go away from the tip and reaches a maximum near the yield curve. To see this note that on the crack surface  $P = \frac{\sqrt{3}}{2}\sigma_Y$  (cf. Eq. (3)). On the yield curve we use Eq. (4) and the Huber-von Mises criterion together to solve the angular dependence of the hydrostatic tension in units of  $\sigma_Y$ . It attains a maximal value of  $\sqrt{3}\sigma_Y$  and is considerably higher than  $\frac{\sqrt{3}}{2}\sigma_Y$  for a wide range of angles. On the other hand the linear-elastic solution (4) implies a monotonically decreasing  $P$  outside the yield curve. We thus expect  $P$  to *attain its maximum value near the yield curve*. This conclusion is fully supported by finite elements method calculations, cf. [16]. Finally, since the nucleation occurs when  $P$  exceeds a threshold  $P_c$ , this threshold is between the limit values found above, i.e.  $\frac{\sqrt{3}}{2}\sigma_Y < P_c < \sqrt{3}\sigma_Y$ . The void will thus appear at a typical distance  $\xi_c$ , see Fig. 2. An immediate consequence of the above discussion is that  $\xi_c$  is related to the crack length via:

$$\xi_c \sim \frac{K_I^2}{\sigma_Y^2} \sim \left(\frac{\sigma^\infty}{\sigma_Y}\right)^2 L. \quad (5)$$

Note that  $\xi_c$  is not a newly found length scale; it is the well known scale of the plastic zone [17]. Its identification with the cross-over length between two scaling behaviors of the crack roughening is however new. This stems from the proposition that positive correlations appear only between the positions of nucleated voids. Below  $\xi_c$  one enters the regime of plastic processes whose

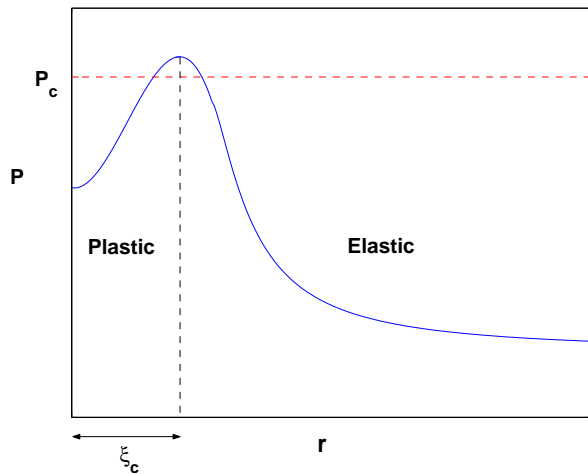


FIG. 2: A forward direction profile of the hydrostatic tension  $P$  in units of  $\sigma_y$ . On the crack  $P = \sqrt{3}/2$  and it attains a maximum of  $\sqrt{3}$  on the yield curve. The threshold line indicates a value of  $P_c$  such that  $\frac{\sqrt{3}}{2} < P_c < \sqrt{3}$ . The typical length  $\xi_c$  is shown. Other directions exhibit qualitatively similar profiles.

theory is far from being settled. We should also comment that it is possible that positive correlations appear even below the scale of the plastic zone since experiments indicate that several voids nucleate within the plastic zone [12, 13]. We should therefore consider the estimate in Eq. (5) as an upper bound on  $\xi_c$ . Finally, the fact that the plastic zone size scales with  $K_I$  as proposed in Eq. (5) results from the assumption of perfect plasticity, i.e. that  $\sigma_y$  is independent of the state of deformation and its history. This is *not* true for real materials; usually  $\sigma_y$  is not sharply defined; it can increase with plastic deformations [14]. This phenomenon, known as “work-hardening” or “strain-hardening”, might introduce other dependencies on  $K_I$  and include other length scales that are related to the plastic deformations. We do not take such issues into account in this simple model.

Naturally, the precise location of the nucleating void will experience a high degree of stochasticity due to material inhomogeneities. Since we do not know from first principles the probability distribution for void formation, we consider in our model below two possible distribution functions. In all cases nucleation cannot occur if  $P < P_c$ . For  $P > P_c$  the void occurs with probability

$$P \propto P - P_c, \quad (6)$$

$$P \propto \exp[\alpha(P - P_c)] - 1. \quad (7)$$

In the exponential case we considered two different values of  $\alpha$ . In Fig. 3 we show three such pdf’s as they appear for a perfectly straight crack. We note that these distributions are symmetric about the forward direction. Nevertheless they have sufficient width to allow deviations from forward growth. These deviations will be re-

sponsible later for the roughening of the crack. For comparison examine also the pdf’s for a general crack which are shown in Fig. 6. There the symmetry is lost: correlation to previous steps create a preference for the upward direction. This source of positive correlations is discussed below in greater detail.

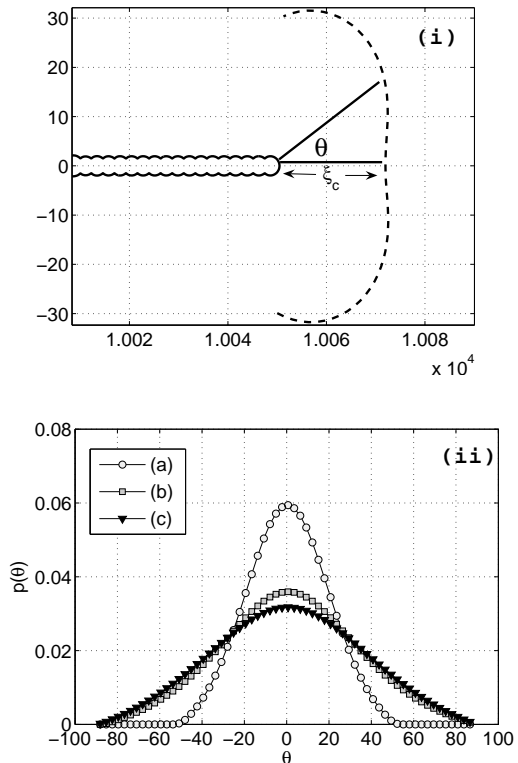


FIG. 3: Panel (i): the tip of a straight crack and the yield curve in front of it.

Panel (ii): three probability distribution functions calculated for the configuration in (i). The abscissa is  $\theta$ , the angle measured from the crack tip as seen in panel (i). The ordinate is the normalized probability (per unit  $\theta$ ) to grow in the  $\theta$  direction. The distributions are symmetric and wide enough to allow deviations from the forward direction. For all the curves  $\frac{\sigma_y}{\sigma_\infty} = 6$ . For curve (a)  $p(\theta) \propto \exp[(P - P_c)] - 1$  and  $\frac{P_c}{\sigma_\infty} = 8$ , for curve (b)  $p(\theta) \propto \exp[0.2(P - P_c)] - 1$  and  $\frac{P_c}{\sigma_\infty} = 6$  and for curve (c)  $p(\theta) \propto P - P_c$  and  $\frac{P_c}{\sigma_\infty} = 6$ .

## B. Crack Propagation

Each growth step in our model is composed of two events. Firstly the material yields near the crack tip, creating a plastic zone with a void growing somewhere at the zone boundary. Secondly the crack tip and the void coalesce. We note that there is a separation of time scales between these two events. The first is slow enough to be governed by a quasi-static stress field. The second event occurs on a shorter time scale. It is clear that we forsake in the one-void model any detailed description

of the geometry on scales smaller than  $\xi_c$ . Any relevant scaling exponent that will be found in this model will refer to roughening on length scales larger than  $\xi_c$ . In experiments it appears that several voids may nucleate before the coalescence occurs, and in the next section we will explore models with two voids ahead of the crack. In the one-void model, the physical process in which the crack coalesces with the multiple voids ahead of it is substituted by a single void coalescence with the crack.

In spite of the simplification in dealing with only one void per step, it was demonstrated in [1] that the one-void model induces positive correlations between consecutive void nucleations, leading eventually to an anomalous roughness exponent larger than 0.5. Clearly, even this simple model requires strong tools to compute the stress field around an arbitrarily shaped crack, to determine at each stage of growth the location of the yield curve and nucleating randomly the next void according to the probability distributions discussed above. In a recent work we have developed precisely the necessary tool in the form of the method of iterated conformal mappings [15].

In the method of iterated conformal mappings one starts with a crack for which the conformal map from the exterior of the unit circle to the exterior of the crack is known. (Below we start with a long crack, in the form of a mathematical branch-cut of length 10000, and  $\xi_c$  is of  $O(10)$ ). We can then grow the crack by little steps in desired directions, computing at all times the conformal map from the exterior of the unit circle to the exterior of the resulting crack. Having the conformal map makes the *exact* calculation of the stress field (for arbitrary loads at infinity) straightforward in principle and highly affordable in practice. The details of the method and its machine implementations are described in full detail in [15]. In the next section we present the theory in great detail for the two-void model, and avoid the repetition here. We should just stress that the method naturally grows cracks with tips of finite curvature, and each step adds on a small addition to the tip, also of a finite size that is controlled in the algorithm.

Having the stress field around the crack we can readily find the yield curve and the physical region in its vicinity where a void can be nucleated. Choosing with any one of the probability distributions described above, we use this site as a pointer that directs the crack tip. We then use the method of iterated conformal mappings to make a growth step to coalesce the tip with the void. Naturally the step sizes are of the order of  $\xi_c$ . In Fig. 4 we present the actual step sizes as computed with the pdf (6), as a function of the crack length. The linearity (in the mean) in  $L$  is obvious. Note that the fluctuations about the mean are strongly dependent on the pdf, and could in principle be used to experimentally deduce the ‘correct’ pdf by reverse engineering. We reiterate that this model forsakes the details of the void structure and all the length scales below  $\xi_c$ . Since we are making *linear* steps below  $\xi_c$ , we anticipate having an artificial scal-

ing exponent  $\zeta = 1$  for scales smaller than  $\xi_c$ . This is clearly acceptable as long as we are mainly interested in the scaling properties on scales larger than  $\xi_c$ .

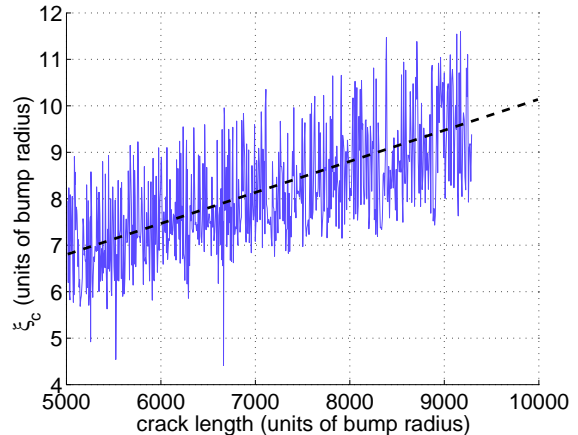


FIG. 4: The step size obtained using pdf (6) (see section II), vs. the crack length. Note that these results agree with Eq.(5) i.e. the step size grows linearly with the crack length. The units here are the ‘bump’ radius which is introduced explicitly in Eq. (47).

In Fig. 5 we present two typical cracks that were grown using this method. Both cracks were initiated from a straight crack of length 10000. The upper crack was grown using the broader exponential pdf of Fig. 6 curve (b). The lower crack was grown with the narrower pdf of Fig. 6 curve (a). Clearly, the upper crack exhibits stronger height fluctuations, as can be expected from the wider pdf and the choice of parameters. For the lower crack forward growth is much more preferred. In the upper crack the positive correlations between successive void nucleation and coalescence events can be seen even with the naked eye. This is precisely the property that we were after. A neat way to see this tendency is in the pdf’s as they are computed on the yields crack for a typical, rather than straight, crack. In Fig. 6 we show these pdf’s for the crack whose yield curve is shown in the upper panel. We see that now the symmetry of the pdf’s is lost, and positive values of  $\theta$  are preferred. This is the source of positive correlations that eventually give rise to the anomalous roughening exponent. This is born out by the measurements of the scaling exponent that we discuss next.

A quantitative measurement of the positive correlations is the roughening exponent, that we compute as follows. Measuring the height fluctuations  $y(x)$  in the graph of the crack, one defines  $h(r)$  according to

$$h(r) \equiv \langle \text{Max} \{y(\tilde{x})\}_{x < \tilde{x} < x+r} - \text{Min} \{y(\tilde{x})\}_{x < \tilde{x} < x+r} \rangle_x. \quad (8)$$

For self-affine graphs the scaling exponent  $\zeta$  is defined via the scaling relation

$$h(r) \sim r^\zeta. \quad (9)$$



FIG. 5: Two typical cracks generated with our model. Note the different scales of the abscissa and ordinate, and that the lower crack had been translated by -300. The upper crack exhibits two decades of self-affine scaling with a Hurst exponent 0.64. The lower crack has smaller standard deviation and therefore a shorter scaling range. Nevertheless it appears that in its shorter scaling range it exhibits an exponent that is very close to the upper crack.

In Fig. 7 we present a typical log-log plot of  $h(r)$  vs.  $r$ , in this case for the two cracks in Fig. 5 with power-law fits of  $\zeta = 0.64$  and  $0.68$  respectively. Indeed as anticipated from the visual observation of Fig. 5 the exponent is higher than 0.5. It turned out that all the cracks grown by our algorithm gave rise to scaling plots in which a scaling range with  $\zeta = 0.66 \pm 0.03$  is clearly seen. When the pdf allowed for a sizeable standard deviation, the cracks gave a very nice scaling plot with at least two decades of clear anomalous scaling. When the standard deviation was small, the scaling range was more meager, as seen in Fig. 7. It is interesting to stress that the anomalous scaling exponent appears insensitive to the pdf used (although the extent of the scaling range clearly depended on the pdf). We note that our measured scaling exponents are very close to the exponents observed in 2-dimensional experiments. (Of course we cannot expect a 2-dimensional theory to agree with 3-dimensional experiments - the scaling exponents are, as always, dimension-dependent). In addition the value of  $\xi_c$  does not effect the scaling properties of a crack, i.e. it doesn't seem to matter how long the step is, so long as a wide distribution of angles is allowed.

Growing directly at the tip of the crack results in a very strong preference for the forward direction, meaning that a step up will most likely be followed by a step down, and vice versa, as shown in [18]. The introduction of the physics of the plastic zone results in creating a finite distance away from the tip to realize the next growth step. Another crucial issue is the existence of long range correlations. Since this aspect was not made clear so far, we turn now to a discussion of the origin of power law correlations.

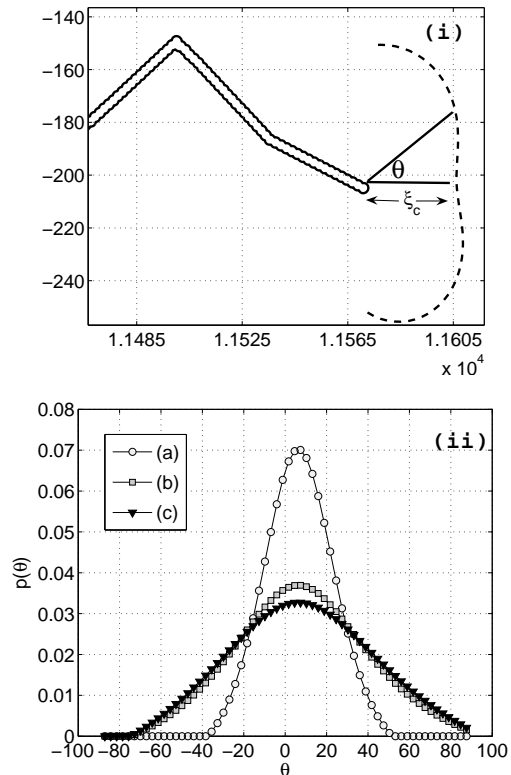


FIG. 6: Panel (i): the tip of a “rough” crack and the yield curve in front of it. Panel (ii): three probability distribution functions calculated for the configuration in panel (i). The abscissa is  $\theta$ , the angle measured from the crack tip as seen in panel (i). The ordinate is the normalized probability (per unit  $\theta$ ) to grow in the  $\theta$  direction. The pdf's are those used in Fig. 3, using the same parameters. Note the upward preference in all the pdf's due to the broken symmetry.

### III. LONG RANGE POSITIVE CORRELATIONS IN FRACTURE

The fact that the cracks generated by our model appear self-affine with Hurst exponent  $\zeta > 0.5$  implies that the physical mechanism underlying the crack growth is a long range positive correlation process. We can gain intuition about the origin of the long range correlations by employing some known analytic results. Consider a long mode I straight crack spanning the interval  $[-L, 0]$ . Suppose now that the crack shape is perturbed by a small out of plane fluctuation of the form  $\epsilon\psi(x)$ , where  $\epsilon > 0$  is small. In the presence of the perturbation the crack attains a small shear component  $K_{II} \neq 0$  at its tip. A first order perturbation analysis in the amplitude  $\epsilon$  reveals that [19]

$$K_{II} \sim -\epsilon \int_{-\infty}^0 \frac{\partial_x [\sigma_{xx}^{(0)}(x, 0)\psi(x)]}{\sqrt{-x}} dx, \quad (10)$$

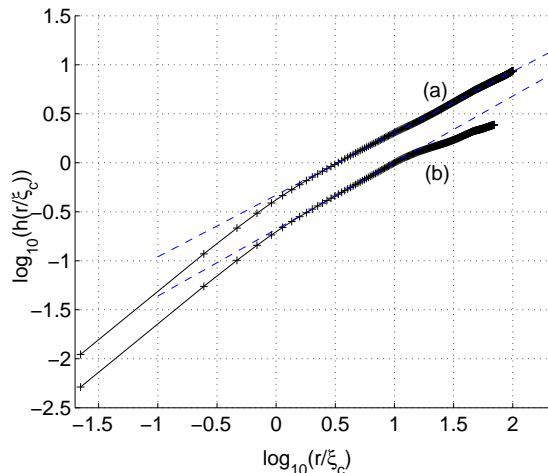


FIG. 7: Calculation of the anomalous roughening exponent. The slopes of the dotted lines are 0.64 for the upper plot (curve a) and 0.68 for the lower (curve b). Note that the initial scaling with slope 1 is relevant for length scales smaller than  $\xi_c$ . This scaling is unphysical, resulting from our algorithm that connects the crack tip to a void by a straight line.

where the superscript in  $\sigma_{xx}^{(0)}(x, 0)$  refers to the solution in the absence of a perturbation. Note that due to the fact that the crack is long we could set the lower limit of integration to  $-\infty$ . Let us consider a positive perturbation  $\psi(x)$  that is symmetric around  $-r$  and decays to zero at a typical distance  $\delta$  from  $-r$ . Since in our configuration  $\sigma_{xx}^{(0)}(x, 0) = -\sigma^\infty$  for  $x < 0$ , it is straight forward to show that Eq. (10) yields

$$K_{II} \sim -\frac{\sigma^\infty \epsilon \delta}{r^{3/2}}, \quad (11)$$

for  $r \gg \delta$ . Note that  $K_{II}$  is *negative*. In order to understand the effect of the perturbation on the probability distribution function for the next void nucleation in our model, we recall that this probability is determined by the hydrostatic tension  $P \equiv \frac{1}{2} \text{Tr} \sigma$ . In the case of a pure tensile stress,  $K_{II} = 0$ ,  $P$  is symmetric around  $\theta = 0$  and the probabilities of nucleating a void at positive or negative angles are the same. In the presence of a small negative shear component,  $K_{II} < 0$ , this picture changes. The maximal hydrostatic tension is obtained at

$$\theta_{max} \sim -\frac{K_I}{K_{II}}. \quad (12)$$

Since to first order in  $\epsilon$  the mode I stress intensity factor  $K_I \sim \sigma^\infty \sqrt{L}$  is unchanged [19], we obtain that the peak of the distribution is shifted from zero to

$$\theta_{max} \sim \frac{\epsilon \delta}{L^{1/2} r^{3/2}} > 0. \quad (13)$$

This relation shows that as a result of a positive perturbation in the crack shape at a distance  $r$  behind its tip the

probability to nucleate a void at a positive angle relative to the forward direction is *higher* than the probability to nucleate a void at a negative angle. Moreover, this positive correlation is long ranged, decaying as  $r^{-3/2}$ .

The presence of long range correlations is reassuring, since they are a must for the existence of a roughening exponent larger than 0.5. Note however that the above result does not determine in any direct way the numerical value of the roughening exponent itself. The actual exponent results from the cumulative effect of many height fluctuations, and at present we do not have an analytic theory predicting the numerical value of this exponent. Contrary to self similar fractal growth patterns, where the fractal dimension  $D$  can be computed from the knowledge of the first Laurent coefficient of the conformal map [20], in self affine graphs it is not obvious how to extract the roughening exponent from the properties of the conformal map. At present we are bound to the laborious process of actually growing the crack and measuring the exponent. Needless to say this is theoretically unsatisfactory, and new ideas on this issue should be very welcome.

#### IV. TWO-VOID MODELS: MATHEMATICAL FORMULATION

In this section we address the physical process of nucleation of a second void in front of the crack tip. To improve upon the one-void model we need to develop techniques to compute the exact stress field around a crack with one void ahead (or a crack with two voids ahead, etc.). Clearly, methods based on conformal maps from singly connected regions (i.e. the unit circle) cannot suffice for this purpose. Since conformal map techniques from doubly or multiply connected regions are far less familiar, and since the computation of stress field around doubly connected regions is interesting by itself, we present the necessary techniques in some detail. Considerable attention will be paid to the accuracy and the efficiency of the calculation. In subsection IV B we review the basis of the relevance of conformal maps to the solution of the bi-Laplace equation. This goes back to Mushkelishvili's series-expansion method [21]. We extend Mushkelishvili's method to doubly connected regions, using conformal maps from the annulus to the required doubly connected region. In Appendix A we elaborate the case of two circular holes. This case is solvable analytically using bipolar coordinates [24], and therefore provides a unique testing ground for the precision of our method in a limiting case.

In this section we solve for the stress field in an unbounded planar doubly connected region. Such calculations exist in the literature; one general method is known as the Schwarz alternating method. In this method one solves the simply connected problems successively and superimposes them in such a way that the boundary conditions are satisfied when the procedure has converged (see for example [23]). We will assess our method by com-



paring with an analytical solution for two equally sized circular holes using bipolar coordinates [24]. Our method is quite general, allowing us to solve for the stress field in any doubly connected region by explicitly solving the elastic equations in a doubly connected geometry. The advantages of our method are that it allows freedom in choosing the shapes of the boundaries and it allows calculation of the stress field near highly singular shapes such as long cracks. The method can be implemented to very high precision as will be shown below.

#### A. Equilibrium equations for the stress field in a doubly connected infinite medium.

The theory of elastostatic fracture mechanics in brittle continuous media is based on the equilibrium equations for an isotropic elastic body [25]

$$\frac{\partial \sigma_{ij}}{\partial x_j} = 0. \quad (14)$$

For in-plane modes of fractures, i.e. under plane-stress or plane-strain conditions, one introduces the Airy stress potential  $U(x, y)$  such that

$$\sigma_{xx} = \frac{\partial^2 U}{\partial y^2} ; \sigma_{xy} = -\frac{\partial^2 U}{\partial x \partial y} ; \sigma_{yy} = \frac{\partial^2 U}{\partial x^2} . \quad (15)$$

Thus the set of Eq. (14), after simple manipulations, translate to a Bi-Laplace equation for the Airy stress potential  $U(x, y)$  [25]

$$\Delta \Delta U(x, y) = 0 , \quad (16)$$

with the prescribed boundary conditions on the crack and on the external boundaries of the material. At this point we choose to focus on the case of uniform remote loadings and traction-free crack boundaries. This choice, although not the most general, is of great interest and will serve to elucidate our method. Other solutions may be obtained by superposition. Thus, the boundary conditions at infinity, for the two in-plane symmetry modes of fracture, are presented as

$$\begin{aligned} \sigma_{xx}(\infty) = 0 ; \sigma_{yy}(\infty) = \sigma^\infty ; \sigma_{xy}(\infty) = 0 & \text{ Mode I} \\ \sigma_{xx}(\infty) = 0 ; \sigma_{yy}(\infty) = 0 ; \sigma_{xy}(\infty) = \sigma^\infty & \text{ Mode II} . \end{aligned} \quad (17)$$

In addition, the free boundary conditions on both boundaries (of crack and void) are expressed as

$$\sigma_{xn}(s) = \sigma_{yn}(s) = 0 , \quad (18)$$

where  $s$  is the arc-length parametrization of the boundaries and the subscript  $n$  denotes the out-ward normal direction.

The solution of the Bi-Laplace equation can be written in terms of *two* analytic functions  $\phi(z)$  and  $\eta(z)$  as

$$U(x, y) = \Re[\bar{z}\phi(z) + \eta(z)] . \quad (19)$$

In terms of these two analytic functions, using Eq. (15), the stress components are given by

$$\begin{aligned} \sigma_{yy}(x, y) &= \Re[2\phi'(z) + \bar{z}\phi''(z) + \eta''(z)] \\ \sigma_{xx}(x, y) &= \Re[2\phi'(z) - \bar{z}\phi''(z) - \eta''(z)] \\ \sigma_{xy}(x, y) &= \Im[\bar{z}\phi''(z) + \eta''(z)] . \end{aligned} \quad (20)$$

In order to compute the full stress field one should first formulate the boundary conditions in terms of the analytic functions  $\phi(z)$  and  $\eta(z)$ . The boundary conditions Eq. (18) can be rewritten, using Eq. (15), as [21]

$$\partial_t \left[ \frac{\partial U}{\partial x} + i \frac{\partial U}{\partial y} \right] = 0 . \quad (21)$$

Where  $\partial_t$  is the tangential derivative along the boundaries. Condition (21) must hold for each of the two boundaries separately. Note that we do not have enough boundary conditions to determine  $U(x, y)$  uniquely. In fact we can allow in Eq. (19) arbitrary transformations of the form

$$\begin{aligned} \varphi &\rightarrow \varphi + iCz + \gamma \\ \psi &\rightarrow \psi + \tilde{\gamma} , \quad \psi \equiv \eta' \end{aligned} \quad (22)$$

where  $C$  is a real constant and  $\gamma$  and  $\tilde{\gamma}$  are complex constants. This provides five degrees of freedom in the definition of the Airy potential. It is important to stress that whatever the choice of the five freedoms, the stress tensor is unaffected; see [21] for an exhaustive discussion of this point. We will explain below how to take advantage of these freedoms to make the formulation simpler. When the domain is doubly connected, the traction-free conditions (21) can be written using (19) as

$$\varphi(z) + z\overline{\varphi'(z)} + \overline{\psi(z)} = D_1 \quad \text{for } z \in C_1 \quad (23)$$

and

$$\varphi(z) + z\overline{\varphi'(z)} + \overline{\psi(z)} = D_2 \quad \text{for } z \in C_2 \quad (24)$$

where  $C_1$  and  $C_2$  are the two boundary curves, and  $D_1$ ,  $D_2$  are complex constants that are eventually uniquely determined by the solution of the problem. To proceed we represent  $\varphi(z)$  and  $\psi(z)$  in Laurent expansion form. Note that  $\varphi(z)$  and  $\psi(z)$  have a poles inside both the boundaries and therefore do not have a Laurent expansion around infinity which is valid everywhere in the complex plane. But for  $|z| > R$  where  $R$  is a radius that encloses both the boundaries the following expansion is valid since  $\varphi(z)$  and  $\psi(z)$  have no poles in this region.

$$\begin{aligned} \varphi(z) &= \varphi_1 z + \varphi_0 + \varphi_{-1}/z + \varphi_{-2}/z^2 + \dots , \\ \psi(z) &= \psi_1 z + \psi_0 + \psi_{-1}/z + \psi_{-2}/z^2 + \dots . \end{aligned} \quad (25)$$

This form is in agreement with the boundary conditions at infinity that disallow higher order terms in  $z$ . Using the boundary conditions (17), we find

$$\begin{aligned} \varphi_1 &= \frac{\sigma^\infty}{4} ; \quad \psi_1 = \frac{\sigma^\infty}{2} & \text{Mode I} , \\ \varphi_1 &= 0 ; \quad \psi_1 = i\sigma^\infty & \text{Mode II} . \end{aligned} \quad (26)$$

Where one of the freedoms in (22) was used to choose  $\varphi_1$  to be real, using the real constant  $C$  in (22). The four remaining freedoms will allow us later on to fix  $\varphi_0$  and  $\psi_0$  in a convenient way.

### B. Application of conformal maps.

In order to enable the calculation of the stress field around an arbitrarily shaped crack and a void, we conformally map the annulus (having its outer radius set to one, i.e. the annulus is  $\rho < r < 1$ ) onto the required doubly connected domain, see Fig. 8. A well known fact is that simply connected domains can be conformally mapped to any other simply connected domains (relying on the Riemann mapping theorem). However, when dealing with doubly connected domains there is an invariant quantity, called the modulus (sometimes recasted as the extremal distance), which is preserved under conformal mappings. As a result only doubly-connected domains with the same modulus can be connected via a conformal map. For an annulus the conformal modulus is just the ratio of the inner radius and the outer radius, so that for the  $\rho < r < 1$  annulus, the modulus is simply  $\rho$ . For that reason the specific annulus which is taken as the domain to be mapped onto the required crack+void domain cannot be just any annulus, but has to be chosen correctly.

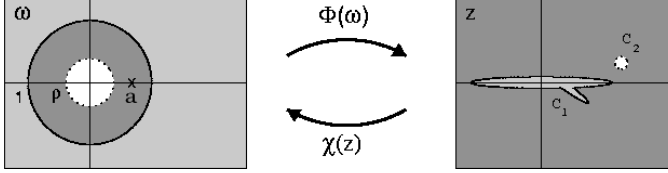


FIG. 8: Illustration of how the conformal map  $\Phi(\omega)$  operates. The unit circle is mapped to  $C_1$  and the inner circle to  $C_2$ . The point  $a$  is mapped to infinity.

Suppose that we have such a conformal map  $\Phi(\omega)$  (examples are presented in the following subsections) that maps the  $\omega$ -annulus domain onto the required physical  $z$ -plane with a crack and a void in front of it. We employ this map to find the solution of the stress field in the physical domain (we also introduce the notation  $\chi(z) \equiv \Phi^{-1}(z)$  for the inverse map). Due to Eq. (19), knowing the solution to the Bi-Laplace equation in the annulus does not immediately provide the solution as the Bi-Laplace equation in the physical domain through a simple application of the conformal map, since in contrast to the Laplace equation, the Bi-Laplace equation is not conformally invariant. Nevertheless, the conformal mapping method can be extended to non-Laplacian problems and provides a clear simplification of the problem since the boundary conditions are much easier to impose on a circular boundary than on the physical boundary. We begin by writing our unknown functions  $\varphi(z)$  and  $\psi(z)$

in terms of the conformal map

$$\varphi(z) \equiv \tilde{\varphi}(\chi(z)) \quad \text{and} \quad \psi(z) \equiv \tilde{\psi}(\chi(z)) \quad (27)$$

Now,  $\tilde{\varphi}(\omega)$  and  $\tilde{\psi}(\omega)$  are just analytical functions in the annulus, apart from a simple pole located at a point which is mapped to infinity in the  $z$ -plane, cf. Fig. 8. Actually, a closer inspection leads us to use the fact that in the  $z$ -plane  $\varphi(z)$  and  $\psi(z)$  have truncated expansions as given in Eqs. (25). Thus, we expect  $\tilde{\varphi}(\omega)$  and  $\tilde{\psi}(\omega)$  to be of the general form

$$\tilde{\varphi}(\omega) = A\Phi(\omega) + \sum_{n=-\infty}^{\infty} \tilde{\varphi}_n \omega^n, \quad (28)$$

and

$$\tilde{\psi}(\omega) = B\Phi(\omega) + \sum_{n=-\infty}^{\infty} \tilde{\psi}_n \omega^n, \quad (29)$$

where for Mode I fracture we can identify

$$A = \varphi_1 = \frac{\sigma_\infty}{4} \quad \text{and} \quad B = \psi_1 = \frac{\sigma_\infty}{2}, \quad (30)$$

just like in Eq. (26) (from here on we use only Mode I boundary conditions at infinity). In contrast to simply connected domains, here we have positive as well as negative powers of  $\omega$  in the expansion. At this point we use the four remaining freedoms ( $\gamma$  and  $\tilde{\gamma}$  in (22)) to choose  $\varphi_0$  and  $\psi_0$  such that

$$\tilde{\varphi}_0 = 0 \quad \text{and} \quad \tilde{\psi}_0 = 0. \quad (31)$$

To impose boundary conditions on the outer (unit) circle of the annulus (i.e.  $|\omega| = 1$ ) we write Eq. (23) in the  $\omega$  plane. This yields (using  $\varepsilon = e^{i\theta}$ )

$$\begin{aligned} \frac{\sigma_\infty}{2} [\Phi(\varepsilon) + \overline{\Phi(\varepsilon)}] + \sum_{n=-\infty}^{\infty} \tilde{\varphi}_n \varepsilon^n + \\ + \frac{\Phi(\varepsilon)}{\Phi'(\varepsilon)} \sum_{n=-\infty}^{\infty} n \tilde{\varphi}_n \varepsilon^{-n+1} + \sum_{n=-\infty}^{\infty} \tilde{\psi}_n \varepsilon^{-n} = D_1. \end{aligned} \quad (32)$$

Imposing boundary conditions on the inner circle of the annulus (i.e.  $|\omega| = \rho$ ) we write Eq. (24) in the  $\omega$  plane. This gives (using  $\omega = \rho\varepsilon = \rho e^{i\theta}$ )

$$\begin{aligned} \frac{\sigma_\infty}{2} [\Phi(\rho\varepsilon) + \overline{\Phi(\rho\varepsilon)}] + \sum_{n=-\infty}^{\infty} \tilde{\varphi}_n \rho^n \varepsilon^n + \\ + \frac{\Phi(\rho\varepsilon)}{\Phi'(\rho\varepsilon)} \sum_{n=-\infty}^{\infty} n \tilde{\varphi}_n \rho^{n-1} \varepsilon^{-n+1} + \sum_{n=-\infty}^{\infty} \tilde{\psi}_n \rho^n \varepsilon^{-n} = D_2. \end{aligned} \quad (33)$$

To proceed we must Fourier Transform the functions  $\Phi(\omega)$  and  $\Phi(\omega)/\Phi'(\omega)$  on the boundaries of the annulus. We use the following notation:

$$\Phi(\varepsilon) = \sum_{n=-\infty}^{\infty} c_n^{\text{out}} \varepsilon^n,$$



$$\begin{aligned}
\frac{\Phi(\epsilon)}{\overline{\Phi'(\epsilon)}} &= \sum_{n=-\infty}^{\infty} b_n^{\text{out}} \epsilon^n, \\
\Phi(\rho\epsilon) &= \sum_{n=-\infty}^{\infty} c_n^{\text{in}} (\rho\epsilon)^n, \\
\frac{\Phi(\rho\epsilon)}{\overline{\Phi'(\rho\epsilon)}} &= \sum_{n=-\infty}^{\infty} b_n^{\text{in}} (\rho\epsilon)^n.
\end{aligned} \tag{34}$$

Here indices with ‘out’ refer to the outer unit circle, and

indices with ‘in’ correspond to the inner circle of radius  $\rho$ . Note that the Fourier coefficients on the inner boundary are not the same as those on the outer boundary, this is because  $\Phi(\omega)$  has a pole inside the annulus. Also note that contrary to the singly connected case, the expansion of  $\Phi(\omega)$  goes to infinity in both positive and negative directions. Inserting Eq. (34) into Eqs. (32) and (33), and gathering powers of  $\epsilon$  we obtain the following infinite set of equations for the coefficients  $\tilde{\varphi}_n$ ,  $\tilde{\psi}_n$  and the unknown constants  $D_1$  and  $D_2$ .

$$\begin{aligned}
\tilde{\varphi}_n + \overline{\tilde{\psi}_{-n}} + \sum_{k=-\infty}^{\infty} k b_{k+n-1}^{\text{out}} \overline{\tilde{\varphi}_k} &= -\frac{\sigma^\infty}{2} (c_n^{\text{out}} + \overline{c_{-n}^{\text{out}}}) + \delta_{n,0} D_1, \quad n = -\infty, \dots, \infty, \\
\tilde{\varphi}_n \rho^n + \overline{\tilde{\psi}_{-n}} \rho^{-n} + \sum_{k=-\infty}^{\infty} k b_{k+n-1}^{\text{in}} \rho^{n+2k-2} \overline{\tilde{\varphi}_k} &= -\frac{\sigma^\infty}{2} (c_n^{\text{in}} \rho^n + \overline{c_{-n}^{\text{in}} \rho^{-n}}) + \delta_{n,0} D_2, \quad n = -\infty, \dots, \infty.
\end{aligned} \tag{35}$$

This set of equations is well-posed and can be solved in various ways. The simplest method is a truncation scheme in which one neglects higher order terms in Eqs. (28) and (29), (taking only a finite subset of coefficients  $\tilde{\varphi}_n$  and  $\tilde{\psi}_n$ ,  $n \neq 0$ ) and just enough equations for solving those coefficients (as well as  $D_1$  and  $D_2$ ). When more and more coefficients  $\tilde{\varphi}_n$  and  $\tilde{\psi}_n$  are taken this scheme converges to the exact solution. The efficiency and rate of convergence of this simple scheme will be examined below.

The calculation of the Laurent expansion form of  $\tilde{\varphi}(\omega)$  and  $\tilde{\psi}(\omega)$  provides the solution of the problem in the  $\omega$ -plane. Still, one should express the derivatives of  $\varphi(z)$  and  $\eta(z)$  in terms of  $\tilde{\varphi}(\omega)$  and  $\tilde{\psi}(\omega)$  and the inverse map  $\chi(z)$  to obtain the solution in the physical  $z$ -plane. This is straightforward:

$$\begin{aligned}
\varphi'(z) &= \tilde{\varphi}'[\chi(z)] \chi'(z) \\
\varphi''(z) &= \tilde{\varphi}''[\chi(z)] [\chi'(z)]^2 + \tilde{\varphi}'[\chi(z)] \chi''(z) \\
\eta''(z) &= \psi'(z) = \tilde{\psi}'[\chi(z)] \chi'(z).
\end{aligned} \tag{36}$$

Upon substituting these relations into Eq. (20) one can calculate the full stress field for an arbitrary doubly connected infinite region.

In Appendix A we present the application of this formalism to the case of two circular holes where the conformal map  $\Phi(\omega)$  and its fourier coefficients are known analytically. In this case one achieves extremely accurate solutions that can be used as testing grounds for the truncation method that is always available even when the fourier coefficients of the conformal map are not given analytically.

### C. Conformal map for arbitrary crack with circular void ahead

Our next task is to find the conformal map  $\Phi(\omega)$  from the interior of the annulus to the exterior of an arbitrarily shaped crack and a void near its tip. We construct this conformal map by composing three auxiliary maps. The properties of the stress maps are as follows:

#### 1. Auxiliary Map 1

Consider the map  $\phi_1(\omega)$  given by,

$$\begin{aligned}
\phi_1(\omega) &= \frac{a\omega - 1}{\omega - a}, \\
a &\in \mathbb{R} \quad \text{and} \quad 0 < a < 1.
\end{aligned} \tag{37}$$

$\phi_1(\omega)$  maps the annulus, i.e.  $\rho < |\omega| < 1$ , onto the exterior of the unit circle and an additional circle on the right as is exemplified in Fig. 9. Note that the unit circle is mapped onto itself and the inner circle is mapped onto the circle on the right. The map  $\phi_1$  has two parameters,  $a$  and  $\rho$ , the first appearing in its definition (the point mapped to infinity), and the other in its domain of definition. Both  $a$  and  $\rho$  are determined by the radius and the center of the rightmost circle (see Fig. 9.) as follows:

$$\begin{aligned}
a &= \frac{x_1 + x_2}{1 + x_1 x_2 + \sqrt{(x_1^2 - 1)(x_2^2 - 1)}}, \\
\rho &= \frac{-1 + x_1 x_2 - \sqrt{(x_1^2 - 1)(x_2^2 - 1)}}{x_1 - x_2},
\end{aligned} \tag{38}$$

where  $x_1$  and  $x_2$  are defined in Fig. 9. Note that the following inequality must hold:

$$0 < \rho < a < 1. \tag{39}$$

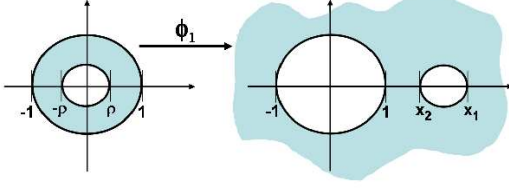


FIG. 9: Illustration of how the conformal map  $\phi_1$  operates.  $\phi_1$  maps the annulus into the exterior of the unit circle and a circle on its right. The unit circle boundary is mapped to itself and the inner circle of radius  $\rho$  is mapped to the circle on the right with radius  $\frac{x_1 - x_2}{2}$ .

The inverse mapping is given by

$$\phi_1^{-1}(z) = \frac{az - 1}{z - a}. \quad (40)$$

Note that the inverse mapping is exactly the same symbol as the direct one.

### 2. Auxiliary Map 2

The second map  $\phi_2(\omega)$  is given by,

$$\phi_2(\omega) = \omega \exp(i\theta). \quad (41)$$

$\phi_2(\omega)$  rotates the plane by an angle  $\theta$  relative to the real axis. The inverse mapping is given by

$$\phi_2^{-1}(z) = z \exp(-i\theta). \quad (42)$$

### 3. Auxiliary Map 3

The role of  $\phi_3$  is to map the exterior of the unit circle to the exterior of an arbitrary crack shape. Assume for now that we have such a map at hand; in subsection IV C 5 we present the explicit derivation of this map using the tools of iterated conformal map. At this point consider the composition of all three maps.

### 4. Composition of the basic maps

The desired mapping  $\Phi(\omega)$  from the annulus to the exterior of a crack and void is given by,

$$\Phi(\omega) = \phi_3(\phi_2(\phi_1(\omega))). \quad (43)$$

The inverse map  $\chi(z)$  is given by,

$$\chi(z) = \Phi^{-1}(z) = \phi_1^{-1}(\phi_2^{-1}(\phi_3^{-1}(z))). \quad (44)$$

The composition of the three auxiliary maps is illustrated in Fig. 10. First  $\phi_1$  is applied and maps the interior of the

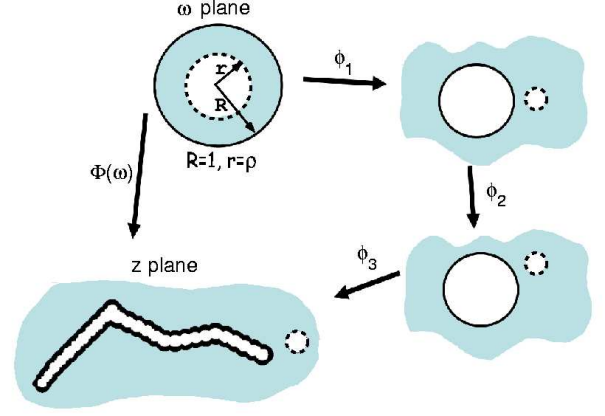


FIG. 10: Illustration of how the conformal map  $\Phi(\omega)$  operates.  $\phi_1$  maps the annulus onto the exterior of two circles,  $\phi_2$  rotates the whole plane and  $\phi_3$  maps the left circle into the desired crack shape, leaving the right circle almost unchanged in its shape.

annulus into the exterior of two circles; then  $\phi_2$  is applied to allow the circle on the right to be rotated with respect to origin. Finally,  $\phi_3$  is applied to map the exterior of the unit circle to the exterior of an arbitrary crack shape. In total,  $\Phi(\omega)$  maps the interior of the annulus to the exterior of a crack and void, such that the outer boundary of the annulus is mapped to the boundary of the crack and the inner boundary is mapped to the void boundary. Notice that since  $\phi_3$  acts on the whole plane, it affects the void, i.e. the circle on the right in Fig. 10, as well as the crack shape. An important property of the mapping we suggest is that for all the configurations we are interested in, applying  $\phi_3$  does not change the shape of the void in an appreciable way, i.e. the void remains almost circular.

In order to create the mapping for a given crack and void configuration one needs a set of points describing the crack's path and the void's radius  $R$  and center  $z_0$ . First one constructs  $\phi_3$  according to the desired crack shape (see section IV C 5). What is left is to obtain the values of  $a$ ,  $\rho$  and  $\theta$  (see auxiliary maps 1 & 2). First we find  $x_1$ ,  $x_2$  and  $\theta$ ,

$$\theta = \arg(\phi_3^{-1}(z_0)). \quad (45)$$

$$\begin{aligned} \frac{x_1 + x_2}{2} &= |(\phi_3^{-1}(z_0))|, \\ \frac{x_1 - x_2}{2} &= |(\phi_3^{-1}(z_0 + R) - \phi_3^{-1}(z_0))|. \end{aligned} \quad (46)$$

One can verify that using the above values for  $x_1$ ,  $x_2$  and  $\theta$ , a void with radius  $R$  and center  $z_0$  is obtained in the  $z$  plane. Substituting  $x_1$  and  $x_2$  in Eq. (38) we obtain the values of  $\rho$  and  $a$ .

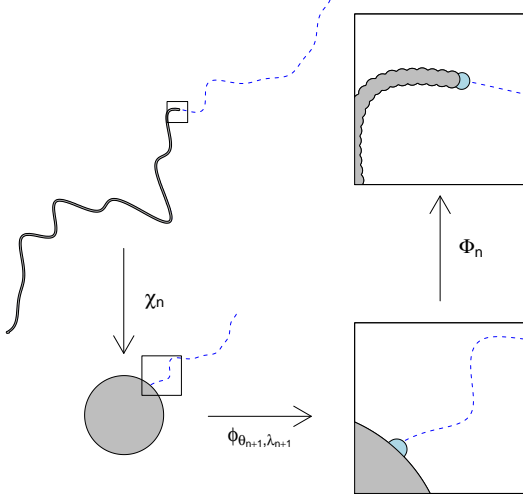


FIG. 11: Example of how to construct the conformal mapping along a line.

### 5. Conformal Map from the unit circle to an arbitrary crack shape

In this subsection we complete the identification of the auxiliary map  $\phi_3$ . For the purpose of being reasonably self-contained we reiterate here some aspects of the machinery of conformal maps. The essential building block in the present application, as in all the applications of the method of iterated conformal maps is the fundamental map  $\phi_{\lambda, \theta}$  that maps the exterior circle onto the unit circle with a semi-circular bump of linear size  $\sqrt{\lambda}$  which is centered at the point  $e^{i\theta}$ . This map reads [22]:

$$\phi_{0, \lambda}(w) = \sqrt{w} \left\{ \frac{(1 + \lambda)}{2w} (1 + w) \right. \quad (47)$$

$$\times \left[ 1 + w + w \left( 1 + \frac{1}{w^2} - \frac{2}{w} \frac{1 - \lambda}{1 + \lambda} \right)^{1/2} \right] - 1 \left. \right\}^{1/2}$$

$$\phi_{\theta, \lambda}(w) = e^{i\theta} \phi_{0, \lambda}(e^{-i\theta} w). \quad (48)$$

The inverse mapping  $\phi_{\theta=0, \lambda}^{-1}$  is of the form

$$\phi_{0, \lambda}^{-1} = \frac{\lambda z - \sqrt{1 + \lambda}(z^2 - 1)}{1 - (1 + \lambda)z^2} z. \quad (49)$$

By composing this map with itself  $n$  times with a judicious choice of series  $\{\theta_k\}_{k=1}^n$  and  $\{\lambda_k\}_{k=1}^n$  we will construct  $\Phi^{(n)}(\omega)$  that will map the exterior of the circle to the exterior of an arbitrary simply connected shape. To understand how to choose the two series  $\{\theta_k\}_{k=1}^n$  and  $\{\lambda_k\}_{k=1}^n$  consider Fig. 11, and define the inverse map  $\omega = \chi^{(n)}(z)$ . Assume now that we already have  $\Phi^{(n-1)}(\omega)$  and therefore also its analytic inverse  $\chi^{(n-1)}(z)$  after  $n - 1$

growth steps, and we want to perform the next iteration. To construct  $\Phi^{(n)}(\omega)$  we advance our mapping in the direction of a point  $\tilde{z}$  in the  $z$ -plane by adding a bump in the direction of  $\tilde{w} = \chi^{(n-1)}(\tilde{z})$  in the  $w$ -plane. The map  $\Phi^{(n)}(\omega)$  is obtained as follows:

$$\Phi^{(n)}(\omega) = \Phi^{(n-1)}(\phi_{\theta_n, \lambda_n}(\omega)). \quad (50)$$

The value of  $\theta_n$  is determined by

$$\theta_n = \arg[\chi^{(n-1)}(\tilde{z})] \quad (51)$$

The magnitude of the bump  $\lambda_n$  is determined by requiring fixed size bumps in the  $z$ -plane. This means that

$$\lambda_n = \frac{\lambda_0}{|\Phi^{(n-1)}(e^{i\theta_n})|^2}. \quad (52)$$

We note here that it is not necessary in principle to have fixed size bumps in the physical domain. In fact, adaptive size bumps could lead to improvements in the precision and performance of our scheme. We consider here the fixed size scheme for the sake of simplicity, and we will show that the accuracy obtained is sufficient for our purposes. Iterating the scheme described above we end up with a conformal map that is written in terms of an iteration over the fundamental maps (47):

$$\Phi^{(n)}(w) = \phi_{\theta_1, \lambda_1} \circ \dots \circ \phi_{\theta_n, \lambda_n}(w). \quad (53)$$

For the sake of newcomers to the art of iterated conformal maps we stress that this iterative structure is abnormal, in the sense that the order of iterates is inverted with respect to standard dynamical systems. On the other hand the inverse mapping follows a standard iterative scheme

$$\chi^{(n)}(z) = \phi_{\theta_n, \lambda_n}^{-1} \circ \dots \circ \phi_{\theta_1, \lambda_1}^{-1}(z). \quad (54)$$

The algorithm is then described as follows; first we divide the curve into segments separated by points  $\{z_i\}$ . The spatial extent of each segment is taken to be approximately  $\sqrt{\lambda_0}$ , in order to match the size of the bumps in the  $z$ -plane. Without loss of generality we can take one of these points to be at the center of coordinates and to be our starting point. From the starting point we now advance along the shape by mapping the next point  $z_i$  on the curve according to the scheme described above. The resulting map  $\Phi^{(n)}(w)$  is employed as  $\phi_3$  above.

## V. TWO-VOID MODELS: RESULTS AND DISCUSSION

### A. Computational aspects and Precision

The method presented in the previous section has two stages which involve numerical approximation. The first is a numerical Fourier transform of the conformal map (see Eq. 34) and the second is the truncation scheme

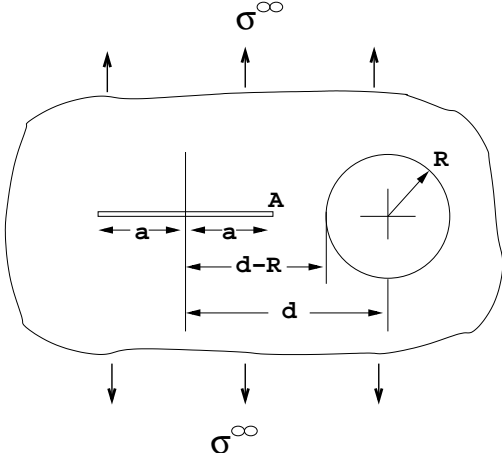


FIG. 12: The configuration of a line with a circle. The comparison of results exhibited in Fig. 13 refers to this configuration.

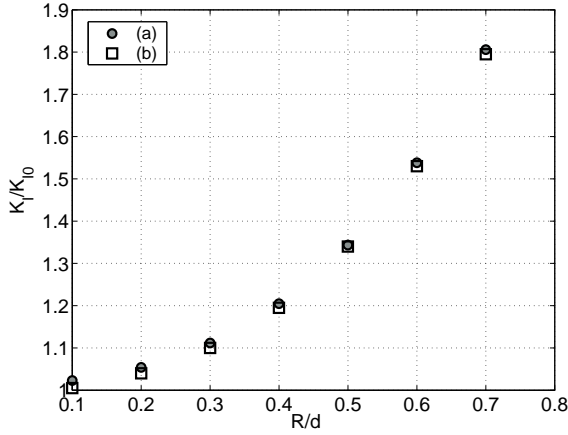


FIG. 13:  $K_I$  for the configuration shown in Fig. 12. Note that the results are normalized by the stress intensity factor with no void i.e  $K_{I0} = \sigma^\infty \sqrt{\pi a}$ . The stress intensity factor was calculated near the point A (i.e. at the tip which is close to the void). The results were calculated for  $a/(d-R) = 0.4$ , varying  $d/R$  in the range  $[0.1, 0.7]$ . Isida's results (b) are shown in squares, and ours (a) in circles.

(see discussion after Eq. (35)). Aside from these two steps the method is analytical. In appendix A we test the truncation scheme (with no numerical Fourier transform) for the case of two circles and find it to be extremely precise. In the next subsection we present a comparison of our method to another theoretical calculation for the straight crack and void geometry. This comparison serves as a testing ground for the numerical Fourier transform and truncation scheme combined.

## B. Stress Intensity Factor for Straight Crack and void

The problem of a crack of length  $2a$  in an infinite domain, subjected to a remote uniaxial load  $\sigma_{yy} = \sigma^\infty$  and traction-free crack faces is considered as the canonical problem in the theory of linear elasticity fracture mechanics. The tensile stress component along the tangent to the crack at the tip is given by [26]

$$\sigma_{\varphi\varphi}(r, 0) = \frac{K_I}{\sqrt{2\pi r}}. \quad (55)$$

$K_I$  is known as the mode I stress intensity factor and for a straight crack it is given by

$$K_I = \sigma^\infty \sqrt{\pi a}. \quad (56)$$

Introducing a void in front of the crack causes an increase in the stress intensity factor. The extent of this increase depends on the void's distance from the crack and its radius (see Fig. 12). The problem of calculating the stress intensity factor for a straight crack and void in front of it has been solved using perturbational analysis by M. Isida [27]. Using our method one can calculate the stress intensity factor for the configuration in Fig. 12 by calculating the stress in a region close to the crack tip and fitting it to the form given in (55). A comparison of our results and those of Isida is given in Fig. 13. We note that Isida's results were extracted by hand from a graph. Also, there are two small differences between our geometry and that of Isida. First, the crack is not strictly a branch cut but has a finite radius of curvature at the tip and second, in our case the inclusion deviates slightly from a perfect circular shape. All these factors together lead to an expected difference of  $\sim 2\%$  between the two methods. We conclude that our results agree (to the expected precision) with those of Isida's and are found to be accurate even in the vicinity of the crack tip.

## C. Stress field near crack tip and void

We now proceed to calculate the full stress field for a configuration of a 'rough' crack with a void. To isolate the effect of the void on the stress field we first calculate the stress for a crack without a void as before. We then add a void and calculate the new stress field. The hydrostatic pressure and yield stress without the void are shown in Fig. 14. The same quantities after the void insertion are shown in Fig. 15.

In theory we could now continue the void nucleation process by inserting a new void in an appropriate point on the new yield curve (the bold curves in Fig. 15). It is obvious however that this will gain us very little. The new yield curve is only locally distorted by the presence of the void, and there is definitely no typical distance of  $2\xi_c$  that could be used to create a decent two-void model.

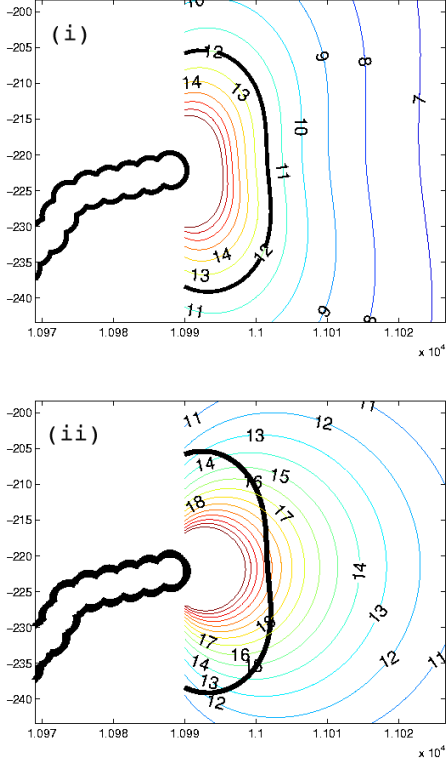


FIG. 14: (color online). Panel (i): field lines of  $\sqrt{J_2}$ , cf. Eq.(1), given in units of  $\sigma^\infty$ . The bold line is the yield curve (i.e.  $\sqrt{J_2}/\sigma^\infty = \sigma_Y/\sigma^\infty = 12$ ). The crack covers the  $x$  interval  $[-10^4, 1.01 \times 10^4]$  and the bump radius is  $\sqrt{\lambda_0} = 2$ . The loading is Mode I with  $\sigma_{yy}(\infty) = \sigma^\infty$ .

Panel (ii): field lines of the hydrostatic pressure,  $P \equiv \frac{1}{2}\text{Tr}\sigma$  for the same crack as the figure above, in units of  $\sigma^\infty$ . The bold line is the yield curve from the previous figure. A reasonable range for  $P_c$  in such a configuration is  $12 \leq \frac{P_c}{\sigma^\infty} \leq 20$ , in accordance with  $\frac{\sqrt{3}}{2}\sigma_Y < P_c < \sqrt{3}\sigma_Y$  (see section II A). Note that  $P_c$  in this range ensures forward growth in the next step.

The root of the problem is that we cannot determine the position of the yield curve based on a fully elastic solution. The correct position of the yield curve and the correct value of the stress on it can only come from a solution of the full elastic-plastic boundary value problem. When growing the first void we assumed that the yield curve calculated from the solution of the fully elastic problem is close to the elasto-plastic yield curve. This assumption works well for the stress field of a crack alone, but produces physically unacceptable results for the stress field of a crack and void. Indeed, finite elements calculations that take plastic flows into account [16] indicate very clearly that the new yield curve is further removed from the first void and certainly does not coincide with the void boundary as it does in our calculation.

The unavoidable conclusion is that the doubly connected conformal calculation that is developed here is useful if one wants to compute the stress field of an elas-

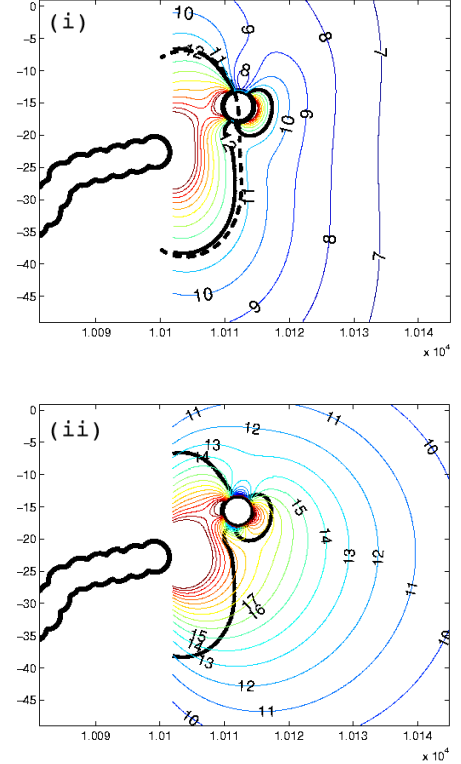


FIG. 15: (color online) The same crack as in Fig. 14 with the addition of a void on the yield curve.

Panel (i): field lines of  $\sqrt{J_2}$  in units of  $\sigma^\infty$ . The bold line is the yield curve with the same value of  $\sigma_Y$  as in Fig. 14 panel (i). The dotted line is the yield curve from Fig. 14 panel (i) i.e. the yield curve for the same crack with no void. The addition of the void creates a very local perturbation of the yield curve.

Panel (ii): field lines of the hydrostatic pressure,  $P \equiv \frac{1}{2}\text{Tr}\sigma$  in units of  $\sigma^\infty$ . The bold line is the yield curve from the figure above. Again the perturbation of the field lines with respect to Fig. 14 panel (ii) is very localized.

tic material in which a hole was inserted in the vicinity of a crack. It cannot be used however to develop an approximate method of taking into account the plastic yields that result in a successive appearance of two voids. The first void can be inserted on the basis of elastic calculations, but the second void cannot be added without a considerably improved consideration of the plastic dynamics. As long as the analytic aspects of plastic dynamics are not elucidated better, the one-void model is proposed as the best available approach to roughening via growth with plastic deformations.

## VI. SUMMARY AND CONCLUSIONS

The crack propagation model presented above, reproduces the experimental appearance of self affine crack rupture lines with an anomalous Hurst exponent. The

long range correlations are created by the stress field which satisfies boundary conditions on the crack's interfaces. The ability to solve the elastic boundary value problem for an arbitrary crack is the basic building block of our theory which enables us to capture these correlations.

To gain a sizeable scaling range with anomalous exponent our model needs to employ a sufficiently wide probability distribution function in the angle  $\theta$  around the tip. While we could not discern a strong dependence of the numerical value of the scaling exponent on the pdf, we do observe a significant dependence of the *extent* of the scaling region. Whenever we found a scaling range the numerical value of the exponent was in the range of  $\zeta = 0.66 \pm 0.03$ .

We have also presented a general method for the calculation of the elastic stress field surrounding a doubly connected region, like a crack and void at its tip, using conformal maps. This method, although not useful for the creation of a two-void model of crack growth, is quite general and can be used for solving different physical problems in doubly connected domains.

### Acknowledgments

This work had been supported in part by European Commission under a TMR grant, the Israel Science Foundation administered by the Israel Academy, and by the Minerva Foundation, Munich Germany. Dr. Katzav's research at the Weizmann Institute of Science is being supported by the Edith and Edward F. Anixter postdoctoral fellowship.

## APPENDIX A: TWO CIRCULAR HOLES

In this section the specific case of two circular holes is solved using the formalism of section IV. For the case of two equally sized circles there exists an analytical so-

lution [24]. In this solution bipolar coordinates are used and a series expansion for the stress components is given in which all the coefficients have a given closed form. We take advantage of the bipolar method to check the precision of our doubly connected method in the two circle limit.

The conformal map for two circular holes is,

$$\Phi(\omega) = \frac{a\omega - 1}{\omega - a}, \quad (A1)$$

$$a \in \mathbb{R} \quad \text{and} \quad 0 < a < 1.$$

$\Phi(\omega)$  maps the annulus, i.e.  $\rho < |\omega| < 1$ , onto the exterior of the unit circle and an additional circle on the right, see Fig. 16. Note that  $\Phi(\omega)$  is the first auxiliary map described in subsection IV C. Since for this case the conformal map has such a simple form, one need not use a numerical FT to obtain its Fourier coefficients, therefore the only approximation left in our method is the

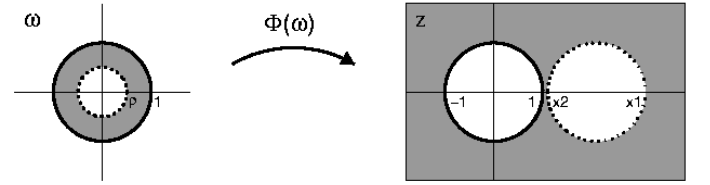


FIG. 16: An example of a conformal mapping of the annulus onto two circular holes. In this example  $x_1 = 1.1$  and  $x_2 = 3.1$ . Note that the unit circle is mapped onto itself, while the  $\rho$ -circle in the  $\omega$ -plane is mapped onto the circle on the right in the  $z$ -plane.

truncation of the functions  $\tilde{\varphi}(\omega)$  and  $\tilde{\psi}(\omega)$  as explained in subsection IV B. As a result the two circle case allows us to isolate and estimate the error associated with the truncation approximation by comparing with the exact results of the bipolar method.

Specializing Eqs. (32)-(33) for  $\Phi(\omega)$  given in Eq (A2) we obtain,

$$\frac{\sigma^\infty}{2} \left( \frac{a\varepsilon - 1}{\varepsilon - a} + \frac{\varepsilon - a}{a\varepsilon - 1} \right) + \sum_{n=-\infty}^{\infty} \tilde{\varphi}_n \varepsilon^n + \frac{1}{1-a^2} \frac{(a\varepsilon - 1)^3}{\varepsilon - a} \sum_{n=-\infty}^{\infty} n \tilde{\varphi}_n \varepsilon^{-n-1} + \sum_{n=-\infty}^{\infty} \tilde{\psi}_n \varepsilon^{-n} = D_1, \quad (A2)$$

and

$$\frac{\sigma^\infty}{2} \left( \frac{a\rho\varepsilon - 1}{\rho\varepsilon - a} + \frac{a\rho - \varepsilon}{\rho - a\varepsilon} \right) + \sum_{n=-\infty}^{\infty} \tilde{\varphi}_n \rho^n \varepsilon^n + \frac{(\rho - a\varepsilon)^2}{1-a^2} \frac{a\rho\varepsilon - 1}{\rho\varepsilon - a} \sum_{n=-\infty}^{\infty} n \tilde{\varphi}_n \rho^{n-1} \varepsilon^{-n-1} + \sum_{n=-\infty}^{\infty} \tilde{\psi}_n \rho^n \varepsilon^{-n} = D_2. \quad (A3)$$

As mentioned above, by expanding these equations in powers of  $\varepsilon$  one can get a well-posed set of equations which can be solved by the truncation procedure. Using

this method we calculated the stress field surrounding two equally sized circles see for example Fig. 16. We then solved the same problem using the fully analytical



bipolar method and found that both methods give the same results to a very high degree of accuracy, i.e. in all space the difference,  $\Delta\sigma$ , between the two methods satisfies

$$\frac{\Delta\sigma}{\sigma^\infty} \simeq 10^{-14} . \quad (\text{A4})$$

This holds in particular for area between the voids which might be expected to give convergence problems. We conclude that the truncation method proves itself very accurate in this limiting case.

- 
- [1] E. Bouchbinder, J. Mathiesen and I. Procaccia, Phys. Rev. Lett. **92**, 245505 (2004), cond-mat/0312669.
  - [2] B.B. Mandelbrot, D.E. Passoja and A.J. Paullay, Nature **308**, 721 (1984).
  - [3] E. Bouchaud, J. Phys. Condens. Matter **9**, 4319 (1997).
  - [4] F. C  lari  , S. Prades, D. Bonamy, L. Ferrero, E. Bouchaud, C. Guillot and C. Marli  re, Phys. Rev. Lett. **90**, 075504 (2003).
  - [5] J. Kert  sz, V.K. Horv  th and F. Weber, Fractals, **1**, 67 (1993).
  - [6] T. Eng  y, K.J. M  l  y, A. Hansen and S. Roux, Phys. Rev. Lett. **73**, 834 (1994).
  - [7] L. I. Salminen, M.J. Alva and K.J. Niskanen, Eur. Phys. J. B. **32**, 369 (2003).
  - [8] J. Feder, *Fractals*, (Plenum, New York, 1988).
  - [9] A. Hansen, E.L. Hinrichsen and S. Roux, Phys. Rev. Lett. **66**, 2476 (1991).
  - [10] A. Hansen and J. Schmittbuhl, Phys. Rev. Lett., **90**, 045504 (2003).
  - [11] S. Ramanathan, D. Ertas, and D. S. Fisher Phys. Rev. Lett. **79**, 873 (1997).
  - [12] E. Bouchaud and F. Paun, Comput. Sci. Eng., **1**, 32 (1999).
  - [13] S. Ciliberto, Private Communication, December 2003.
  - [14] J. Lubliner, *Plasticity Theory*, (Macmillan, New York, 1990).
  - [15] E. Bouchbinder, J. Mathiesen and I. Procaccia, Phys. Rev. E **68**, 026127 (2004), cond-mat/0309523.
  - [16] N. Aravas and R.M. McMeeking, J. Mech. Phys. Solids **33**, 25 (1985).
  - [17] J.R. Rice, J. App. Mech. **35**, 379 (1968).
  - [18] F. Barra, A. Levermann and I. Procaccia, Phys. Rev. E **66**, 066122 (2002), cond-mat/0205132.
  - [19] E. Bouchbinder, H. G. E. Hentschel and I. Procaccia, Phys. Rev. E, **68**, 036601, (2003), nlin.CD/0305021.
  - [20] B. Davidovitch, A. Levermann, I. Procaccia, Phys. Rev. E, **62** R5919 (2000), cond-mat/0008053.
  - [21] N. I. Muskhelishvili, *Some Basic Problems of the Mathematical Theory of Elasticity*, (Noordhoff, 1953).
  - [22] M.B. Hastings and L.S. Levitov, Physica D **116**, 244 (1998).
  - [23] L. Q. Zhang, Z.Q. Yue, C.F. Lee, L.G. Tham and Z.F. Yang, J. Eng. Mech. **129** 1394 (2003).
  - [24] Chih-Bing Ling, J. Appl. Phys. **19** 77, (1947).
  - [25] L.D. Landau and E.M. Lifshitz, *Theory of Elasticity*, 3rd ed. (Pergamon, London, 1986).
  - [26] B. R. Lawn, *Fracture of Brittle Solids* 2nd Edition, (Cambridge University Press, 1998).
  - [27] M. Isida, Eng. Frac. Mech, **2** 61 (1970).